AIAA JOURNAL
Vol. 46, No. 1, January 2008

Turbofan Aft Noise Predictions Based on Lilley's Wave Model

Damiano Casalino* and Mariano Genito†
Italian Aerospace Research Center, 81043 Capua, Italy

DOI: 10.2514/1.32046

To model the sound propagation through the discontinuous flow in a turbofan bypass configuration, a homogeneous linearized Lilley's equation is discretized in the frequency domain by using the Green's function discretization scheme. The main advantage of this third-order wave model, with respect to a conventional second-order model, is that it describes the refraction of an acoustic pressure field without restrictions on the ratio between the acoustic wavelength and the spatial nonuniformity scale of the mean flow. The resulting numerical model can be also applied in the vortex-sheet limit without any treatment of the wake shed from a trailing edge under sound excitation. Three-dimensional numerical solutions of the sound radiation from a bypass duct configuration are compared with analytical results available in the literature. Different cut-on duct modes are considered in the presence of different flow conditions, also including a developing mixing layer instead of an infinitesimal vortex sheet. The influence of an acoustically treated centerbody is also evaluated, as well as the noise scattering effects due to the presence of rigid splices on the afterbody. Additional key aspects of the present study are the use of a cylindrical formulation of the perfectly-matched-layer far-field condition, and the use of an iterative technique to solve the linear system without any observed occurrence of instability waves.

Nomenclature

c	=	speed of sound
G	=	free-space Green's function
i	=	imaginary unit, $\sqrt{-1}$
k	=	acoustic wave number, ω/c_∞
k_r	=	radial duct mode wave number
M	=	Mach number
$\mathcal{M}$	=	Dirichlet-to-Neumann factor
$\boldsymbol{n}$	=	normal unit vector
p	=	pressure
R	=	gas constant
T	=	temperature
U	=	base-flow velocity
u	=	velocity
$\mathcal{Z}$	=	dimensionless wall impedance
α, σ	=	perfectly-matched-layer buffer constants
β	=	Prandtl–Glauert factor, $\sqrt{1-M^2}$
γ	=	ratio of specific heats at constant pressure and volume
η	=	mixing-layer similarity constant
ξ	=	duct mode cut-on ratio $k/(k_r\beta)$
ρ	=	density

Subscripts

0	=	base-flow quantities
∞	=	undisturbed medium properties

Superscripts

$'$	=	perturbation quantities
$\tilde{\cdot}$	=	dimensionless base-flow quantities

I. Introduction

THE development of predictive tools for the design and optimization of acoustically efficient aeroengine nacelles is a competitive topic for aircraft manufacturers.

Even if accurate and robust commercial codes are nowadays available to nacelle designers, there are still two limitations that restrict their industrial exploitation to axisymmetric predictions of inlet noise radiation. The first one is due to the large computational resources required for three-dimensional computations; the second one is due to the use of velocity potential models that are unsuited to compute the sound propagation in a rotational sheared flow. Three-dimensional computations are required, for instance, in the presence of a negatively scarfed intake [1,2] or a circumferentially nonuniform acoustic treatment [3]. Fan noise propagation in a sheared flow occurs close to the bypass nozzle, because of the mixing layer between the secondary and the external flows.

With the objective of reducing the computational effort in both CPU time and memory requirements, and enabling three-dimensional predictions of noise propagation at realistic operating conditions, the first author and coworkers have developed a frequency-domain acoustic propagator based on the Green's function discretization (GFD) of second-order convected wave equations for the acoustic potential [4–6]. Two models have been implemented: the first one, derived by Pierce [7], is valid for background rotational flows, but only for those that vary slowly over the length and time scale of the sound waves (high-frequency approximation); the second model is obtained by linearization of the compressible full potential equation and is therefore only valid for irrotational base flows, until the practical relevance of theoretical extensions to vortical base flows will not be demonstrated [8]. Both these acoustic models, although satisfactory for the prediction of noise radiation from the nacelle intake, are inadequate for the prediction of noise radiation from the bypass duct exhaust, due to the presence of a sheared base flow. Therefore, to extend the predictive capabilities of the GFD code in the presence of an almost unidirectional transversely sheared flow, a third-order wave equation for the acoustic perturbation has been recently implemented and

Presented as Paper 3705 at the 13th AIAA/CEAS Aeroacoustics Conference (28th AIAA Aeroacoustics Conference), Rome, 21–23 May 2007; received 9 May 2007; revision received 28 August 2007; accepted for publication 31 August 2007.

*Senior Research Engineer, Rotorcraft Aerodynamics and Aeroacoustics Laboratory. Member AIAA.

†Research Engineer, Rotorcraft Aerodynamics and Aeroacoustics Laboratory.

partially verified [9]. This equation is obtained by linearizing the Lilley's equation [10] with respect to a stationary flow and seems to be a viable alternative to the solution of linearized Euler equations (LEE) [11]. Indeed, due to the computational cost and to the occurrence of instability waves of hydrodynamic nature in the shear layer that contaminate the acoustic solution, the industrial relevance of the LEE approach for aft noise prediction has been proven only in few cases [12].

A preliminary assessment of the linearized Lilley's wave model for the solution of an edge scattering problem has been recently carried out in [13] by comparing the GFD results with an analytical solution of sound diffraction from a semi-infinite flat plate, and to numerical solutions obtained by using a LEE approach. The goal of the present study is therefore to finalize the verification process of the frequency-domain linearized Lilley's approach by comparing the GFD results with a benchmark analytical solution for a configuration close to a realistic bypass duct. A Wiener–Hopf solution of the sound radiation from a semi-infinite unflanged annular duct with infinite centerbody, recently obtained by Gabard and Astley [14] and extended to a lined centerbody by Demir and Rienstra [15], has been considered. All the cases addressed in [14] have been successfully reproduced, but only a subset of them is herein reported. Both axisymmetric and three-dimensional computations have been performed with a twofold aim in mind: verifying the discretization scheme in both cases, and obtaining, through axisymmetric computations, grid-independent reference solutions for the three-dimensional results.

The paper is organized as follows. In Sec. II, the governing equations are briefly presented. The key elements of the numerical method are outlined in Sec. III, with emphasis on the perfectly-matched-layer (PML) formulation for an annular buffer in the far field, which represents the only original contribution of this work with respect to previous works by the authors. In Sec. IV, the numerical verification process is outlined and some results showing the effects of a spliced liner on the afterbody and of a mixing layer are presented. Finally, the main conclusions of the present study and future extensions of the proposed approach are drawn in Sec. V.

II. Aeroacoustic Model

By rearranging the mass and linear momentum conservation equations in a compressible fluid and neglecting viscous effects, Lilley [10] obtained the following equation:

$$\frac{\mathrm{D}}{\mathrm{D}t}\left[\frac{\mathrm{D}^2\Pi}{\mathrm{D}t^2}-\frac{\partial}{\partial x_j}\left(c^2\frac{\partial\Pi}{\partial x_j}\right)\right]+2\frac{\partial u_k}{\partial x_j}\frac{\partial}{\partial x_k}\left(c^2\frac{\partial\Pi}{\partial x_j}\right)=-2\frac{\partial u_j}{\partial x_k}\frac{\partial u_i}{\partial x_j}\frac{\partial u_k}{\partial x_i} \tag{1}$$

where $\Pi=(1/\gamma)\,\ell_n(p/p_0)$, and p, ρ, T, c, and u_i denote the flow pressure, density, temperature, sound speed, and Cartesian velocity components, respectively. The fluid is assumed to be an ideal gas so that $c^2=\gamma p/\rho=\gamma RT$, where γ and R are the ratio of specific heats and the gas constant, respectively.

If the flow variables are split into time-independent base-flow quantities and fluctuating perturbation quantities, it is possible to recast Eq. (1) into the form of an acoustic analogy equation in which a third-order wave operator acts on the pressure perturbation $\Pi'=(1/\gamma)p'/p_0$ and the remaining terms, shifted at the right-hand side, are treated as aeroacoustic sources, i.e.,

$$\frac{\mathrm{D}_0}{\mathrm{D}t}\left[\frac{\mathrm{D}_0^2\Pi'}{\mathrm{D}t^2}-\frac{\partial}{\partial x_j}\left(c_0^2\frac{\partial\Pi'}{\partial x_j}\right)\right]+2\frac{\partial u_k}{\partial x_j}\frac{\partial}{\partial x_k}\left(c_0^2\frac{\partial\Pi'}{\partial x_j}\right)=S \tag{2}$$

where p_0, T_0, c_0, U_i denote base-flow quantities, $\mathrm{D}_0/\mathrm{D}t$ is the base-flow Lagrangian derivative, and the term at the right-hand side is given by

$$\begin{aligned}S=&-\left[3\frac{\mathrm{D}_0^2}{\mathrm{D}t^2}u_j'\frac{\partial}{\partial x_j}+3\frac{\mathrm{D}_0}{\mathrm{D}t}\left(u_j'\frac{\partial}{\partial x_j}\right)^2+\left(u_j'\frac{\partial}{\partial x_j}\right)^3\right]\Pi'\\&+\frac{\mathrm{D}_0}{\mathrm{D}t}\frac{\partial}{\partial x_j}\left(c'^2\frac{\partial\Pi'}{\partial x_j}\right)+u_k'\frac{\partial^2}{\partial x_k\partial x_j}\left(c^2\frac{\partial\Pi'}{\partial x_j}\right)\\&-2\frac{\partial U_k}{\partial x_j}\frac{\partial}{\partial x_k}\left(c'^2\frac{\partial\Pi'}{\partial x_j}\right)-2\frac{\partial u_k'}{\partial x_j}\frac{\partial}{\partial x_k}\left(c^2\frac{\partial\Pi'}{\partial x_j}\right)\\&-2\frac{\partial U_j}{\partial x_k}\frac{\partial U_i}{\partial x_j}\frac{\partial u_k'}{\partial x_i}-2\frac{\partial U_j}{\partial x_k}\frac{\partial u_i'}{\partial x_j}\frac{\partial U_k}{\partial x_i}-2\frac{\partial U_j}{\partial x_k}\frac{\partial u_i'}{\partial x_j}\frac{\partial u_k'}{\partial x_i}\\&-2\frac{\partial u_j'}{\partial x_k}\frac{\partial u_i'}{\partial x_j}\frac{\partial U_k}{\partial x_i}-2\frac{\partial u_j'}{\partial x_k}\frac{\partial u_i'}{\partial x_j}\frac{\partial u_k'}{\partial x_i}\end{aligned} \tag{3}$$

Because Eq. (3) contains terms which are linear in the velocity perturbation $\boldsymbol{u}'$, it is not possible to unambiguously determine what part of the perturbation field is associated with the sound propagation and what part drives the sound generation process. In many practical situations, however, the base flow can be approximated as a unidirectional transversely sheared flow and the linear terms in Eq. (3) can be neglected. In this case, the linearized Lilley's Eq. (2) exhibits a clearer separation between sound propagation and generation.

In the framework of jet mixing noise prediction, a significant interest is devoted to the analysis and numerical modeling of the different forms in which the source terms arising in Lilley's acoustic analogy can be recast [16–19]. In the present work, however, the noise excitation is only prescribed via a boundary condition on a duct inlet, and the only interest is in the wave operator and not in the source terms. Therefore, by assuming harmonic perturbations of radian frequency ω and making use of the base-flow Lagrangian derivative $\mathrm{D}_0/\mathrm{D}t=-\mathrm{i}\,\omega+U_i\partial/\partial x_i$, Eq. (2) takes the following homogeneous form:

$$\begin{aligned}&\mathrm{i}\,k^3\Pi'-3k^2\tilde{U}_i\frac{\partial\Pi'}{\partial x_i}-3\,\mathrm{i}\,k\tilde{U}_i\tilde{U}_j\frac{\partial^2\Pi'}{\partial x_i\partial x_j}-3\,\mathrm{i}\,k\left(\tilde{U}_j\frac{\partial\tilde{U}_i}{\partial x_j}\right)\frac{\partial\Pi'}{\partial x_i}\\&+\tilde{U}_k\frac{\partial}{\partial x_k}\left(\tilde{U}_i\tilde{U}_j\frac{\partial^2\Pi'}{\partial x_i\partial x_j}\right)+\tilde{U}_k\frac{\partial}{\partial x_k}\left[\left(\tilde{U}_j\frac{\partial\tilde{U}_i}{\partial x_j}\right)\frac{\partial\Pi'}{\partial x_i}\right]\\&+\mathrm{i}k\frac{\partial\tilde{T}}{\partial x_j}\frac{\partial\Pi'}{\partial x_j}+\mathrm{i}k\tilde{T}\frac{\partial^2\Pi'}{\partial x_j^2}-\tilde{U}_k\frac{\partial}{\partial x_k}\left(\frac{\partial\tilde{T}}{\partial x_j}\frac{\partial\Pi'}{\partial x_j}+\tilde{T}\frac{\partial^2\Pi'}{\partial x_j^2}\right)\\&+2\frac{\partial\tilde{U}_k}{\partial x_j}\left[\frac{\partial\tilde{T}}{\partial x_k}\frac{\partial\Pi'}{\partial x_j}+\tilde{T}\frac{\partial^2\Pi'}{\partial x_k\partial x_j}\right]=0\end{aligned} \tag{4}$$

where $k=\omega/c_\infty$ is the acoustic wave number, and $\tilde{U}_i=U_i/c_\infty$ and $\tilde{T}=T_0/T_\infty$ are base-flow quantities made dimensionless by freestream reference conditions. As a matter of generality, the three-dimensional base-flow notation has been retained, even when the base flow is not exactly a unidirectional transversely sheared base flow, as for the mixing-layer case.

The set of governing equations is completed by an impedance condition on the duct walls, and by a Sommerfeld radiation condition on far-field boundaries. The impedance condition was obtained by Myers [20] under the hypothesis of potential flow and smoothly curved surface. The same boundary condition holds for the acoustic

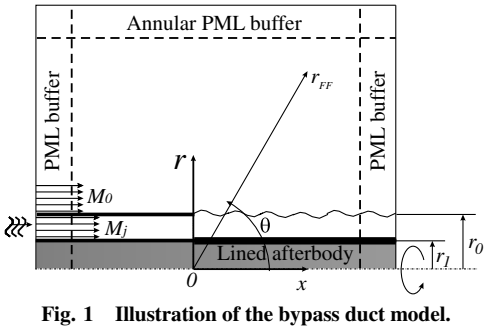

Fig. 1 Illustration of the bypass duct model.

pressure and, in a first-order approximation, for the logarithmic pressure perturbation Π', i.e.,

$$k\frac{\partial \Pi'}{\partial x_i}\hat{n}_i + \frac{1}{\mathcal{Z}}\left\{k + \mathrm{i}\,\tilde{U}_j\frac{\partial}{\partial x_j} - \mathrm{i}\hat{n}_i\left(\frac{\partial \tilde{U}_i}{\partial x_j}\hat{n}_j\right)\right\} \times \left(\mathrm{i}\,k\Pi' - \tilde{U}_i\frac{\partial \Pi'}{\partial x_i}\right) = 0 \tag{5}$$

where $\mathcal{Z}$ is the dimensionless acoustic impedance ($-\mathrm{i}\,\omega t$ convention) and $\hat{\boldsymbol{n}}$ is the normal unit vector pointing into the wall. In the hard-wall limit [$\mathrm{Re}(\mathcal{Z}) \to \infty$], the zero normal derivative condition for the pressure perturbation can be obtained.

The Sommerfeld radiation condition is a Robin-type condition in which the Dirichlet-to-Neumann (DtN) factor is obtained by considering a plane wave propagating in a uniform flow, and by approximating the radiation vector with the outward normal unit vector $\hat{\boldsymbol{n}}$. It reads

$$\frac{\partial \Pi'}{\partial x_i}\hat{n}_i - \mathcal{M}\Pi' = 0 \tag{6}$$

where

$$\mathcal{M} = \frac{\mathrm{i}\,k}{\beta^2\sqrt{\tilde{T}}}(-M_n + \sqrt{M_n^2 + \beta^2}) \tag{7}$$

is the DtN factor, $\boldsymbol{M}_n = \boldsymbol{U}\cdot\hat{\boldsymbol{n}}/c$ is the base-flow Mach number projected on the outward normal direction, and β is the Prandtl–Glauert factor. As discussed in Sec. III, the radiation condition is used in connection with a PML technique to attenuate the outgoing acoustic waves and minimize inward spurious reflections, while reducing the extension of the buffer zone.

III. Numerical Method

In this section, the underlying features of the numerical method are briefly reviewed. The only novel contribution with respect to previous works [4–6] by the first author and coworkers is the axisymmetric PML formulation for sound attenuation in the radial direction. All the details about the development and validation of the GFD scheme can be found in the referenced papers.

A. Discretization Scheme

The linearized Lilley's Eq. (4) and the boundary conditions (5) and (6), are discretized by using the GFD scheme, following the approach outlined in [9]. The GFD scheme, originally developed to discretize a second-order wave equation for the acoustic velocity potential [4–6], has been recently extended to a third-order wave equation for the pressure perturbation. As a matter of completeness, only the basic derivation steps of the GFD scheme are hereafter outlined.

Consider a generic volume around the point $\mathbf{x}$ in which the acoustic pressure p' satisfies the convected Helmholtz equation, and suppose that the values $p'_m = p'(\mathbf{x}_m)$ are prescribed at a certain number M of neighboring stencil points $\mathbf{x}_m$. By supposing that the local acoustic field is realized by an arbitrary distributions of N elementary sources located at the points $\mathbf{x}_n$, an interpolation formula can be derived from a compatibility condition between the acoustic pressure at the M points and the Helmholtz equation, i.e,

$$p'(\mathbf{x}) = \sum_{m=1}^{M}\sum_{n=1}^{N} G^I_{nm}G(\mathbf{x},\mathbf{x}_n)p'_m \tag{8}$$

where

$$G(\mathbf{x},\mathbf{x}_n) = \exp[\mathrm{i}\,kr(-M_r + \sqrt{M_r^2+\beta^2}/\beta^2)]/(r\sqrt{M_r^2+\beta^2}) \tag{9}$$

is the Green's function of the convected Helmholtz equation and G^I_{nm} is the pseudoinverse ($N > M$) of the influence matrix $G_{mn} \equiv G(\mathbf{x}_m,\mathbf{x}_n)$. Finally, by applying differential operators to

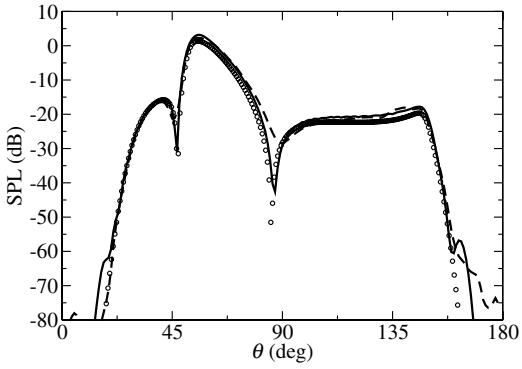

a) Hard-wall afterbody

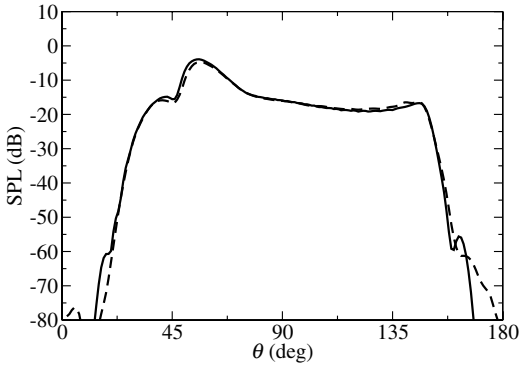

b) Soft-wall afterbody

Fig. 2 Far-field pressure directivity pattern (SPL_D). Comparison between analytical (symbols), axisymmetric GFD results (solid line), and three-dimensional GFD results (dashed line). Mode (17, 2).

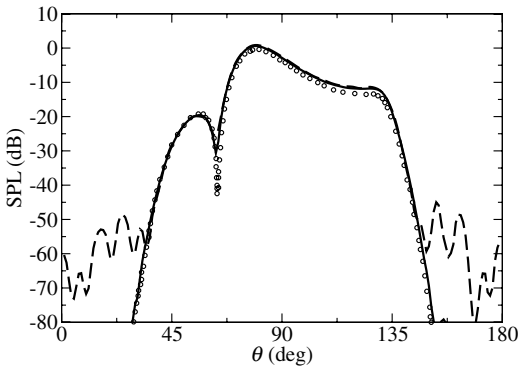

a) Hard-wall afterbody

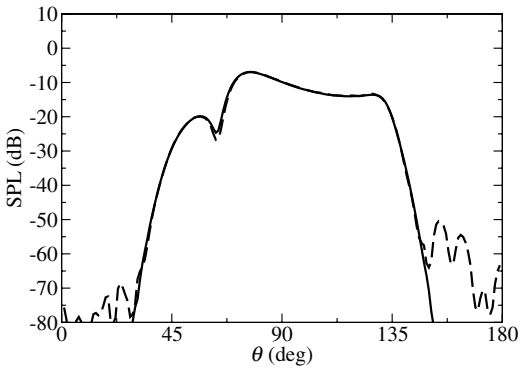

b) Soft-wall afterbody

Fig. 3 Far-field pressure directivity pattern (SPL_D). Comparison between analytical (symbols), axisymmetric GFD results (solid line), and three-dimensional GFD results (dashed line). Mode (24, 2).

Eq. (8), local approximations of the derivatives of $p'(\mathbf{x})$ can be obtained and used to discretize the set of governing equations.

B. Nonreflecting Boundary Conditions

In the present work, PML buffers are used to model nonreflecting sound radiation conditions, and to impose a duct spinning mode at the bypass duct inlet, without affecting the backward outgoing waves generated at the duct opening. The employed PML formulation is the same as that described in [6], but neglecting the base-flow terms in the complex change of variables (λ terms forced to zero). The radiation condition is thus based on the use of a standard PML formulation in conjunction with a radiation condition at the outer boundary of the buffer zone.

The computational domain is obtained by axial extrusion of a two-dimensional Cartesian grid. On the downstream and upstream far-field boundaries, which are normal to the axial direction, the vanishing perturbation condition $\Pi' = 0$ has been imposed. On the cylindrical far-field boundary, a modified form of Eq. (6), obtained by applying a cylindrical PML change of variables to the first-order derivatives, has been used as radiation condition. The PML complex change of variables in the annular buffer is obtained by forcing an evanescent behavior onto the radial component. Thus, denoting as x the axial direction, the full set of PML transformations is given by

$$\frac{\partial_{\mathrm{PML}}}{\partial x} = \alpha_x \frac{\partial}{\partial x}, \qquad \frac{\partial_{\mathrm{PML}}}{\partial y} = \alpha_y \frac{\partial}{\partial y}, \qquad \frac{\partial_{\mathrm{PML}}}{\partial z} = \alpha_z \frac{\partial}{\partial z}$$

$$\frac{\partial^2_{\mathrm{PML}}}{\partial x \partial x} = \alpha_x \alpha_x \frac{\partial^2}{\partial x \partial x}, \qquad \frac{\partial^2_{\mathrm{PML}}}{\partial x \partial y} = \alpha_x \alpha_y \frac{\partial^2}{\partial x \partial y}, \qquad \frac{\partial^2_{\mathrm{PML}}}{\partial x \partial z} = \alpha_x \alpha_z \frac{\partial^2}{\partial x \partial z}$$

$$\frac{\partial^2_{\mathrm{PML}}}{\partial y \partial y} = \left(\alpha_y^2 + \frac{z^2}{r^2}\right)\frac{\partial^2}{\partial y \partial y} + \left(1 - \frac{1}{\alpha_r^2}\right)\alpha_y \alpha_z \frac{\partial^2}{\partial y \partial z} + \left(1 - \frac{1}{\alpha_r}\right)\frac{1}{r}\alpha_y \frac{\partial}{\partial y}$$

$$\frac{\partial^2_{\mathrm{PML}}}{\partial y \partial z} = \alpha_y \alpha_z \frac{\partial^2}{\partial y \partial z}$$

$$\frac{\partial^2_{\mathrm{PML}}}{\partial z \partial z} = \left(\alpha_z^2 + \frac{y^2}{r^2}\right)\frac{\partial^2}{\partial z \partial z} + \left(1 - \frac{1}{\alpha_r^2}\right)\alpha_y \alpha_z \frac{\partial^2}{\partial y \partial z} + \left(1 - \frac{1}{\alpha_r}\right)\frac{1}{r}\alpha_z \frac{\partial}{\partial z} \tag{10}$$

where $r = \sqrt{y^2 + z^2}$, $\alpha_y = \alpha_r y/r$, $\alpha_z = \alpha_r z/r$, $\alpha_x = 1/(1 + \mathrm{i}\sigma_x)$, and $\alpha_r = 1/(1 + \mathrm{i}\sigma_r)$, with σ_x and σ_r denoting the PML damping constant along the axial and radial directions, respectively. To ensure a smoother transition from the physical domain to the axial and radial buffers, the damping factors σ are increased from zero to a maximum value at the external boundary with quadratic law $\sigma = \sigma^{\max} l^2$, where l is a normalized coordinate varying from zero to one in the axial and radial buffers away from the computational domain. In the radial PML buffer, the flow is forced to be uniform and the third-order wave equation is reduced to a second-order convected Helmholtz equation.

The PML condition employed in the bypass duct inlet is based on the splitting between the incident and reflected waves. Therefore, supposing that the outgoing component of Π' satisfies the wave equation, provides the nonhomogeneous wave equation $\mathcal{L}(\Pi') = \mathcal{L}(\Pi'_{\mathrm{inc}})$ that is solved in the PML buffer by employing a wave operator $\mathcal{L}$ in which use of Eq. (10) has been done.

IV. Results and Discussion

In this section, a subset of numerical results obtained by performing the same parametric study as in [14] is presented. The model problem of a coaxial double stream issuing from a semi-infinite annular duct with infinite centerbody, as sketched in Fig. 1, is considered.

Both axisymmetric and three-dimensional computations are carried out. The computational domain is rectangular for the axisymmetric cases and annular for the three-dimensional cases. The origin of the coordinate system is located at the center of the bypass

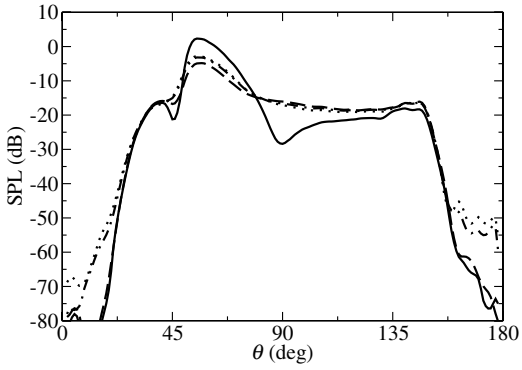

a) Mode (17,2)

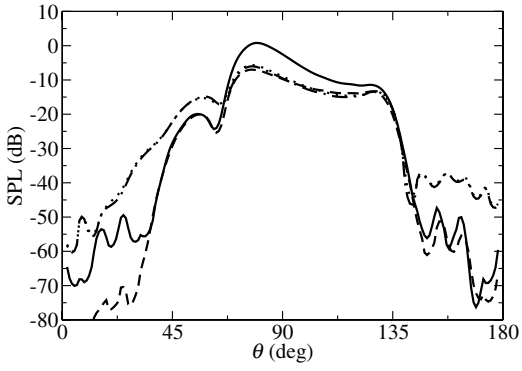

b) Mode (24,2)

Fig. 4 Far-field pressure directivity pattern (SPL_D). Afterbody impedance effects. Hard-wall (solid line), soft-wall (dashed line), small splice thickness (dot-dashed line), large slice thickness (dotted line).

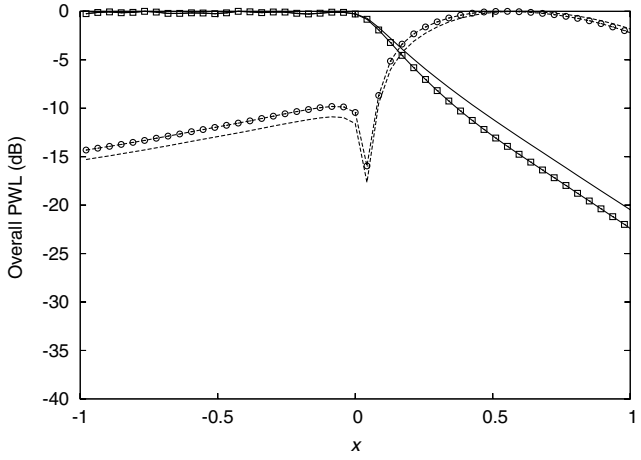

a) Mode (17,2)

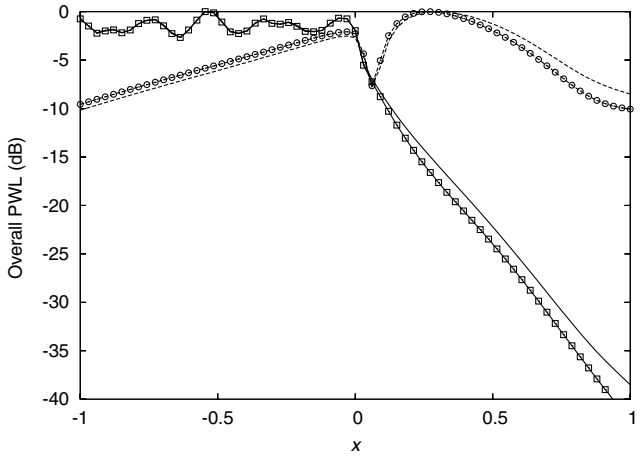

b) Mode (24,2)

Fig. 5 Overall axial power levels. Afterbody impedance effects. Spliced afterbody (lines), zero-splice afterbody (lines + symbols). Inner cylinder (solid line), outer cylinder (dashed line).

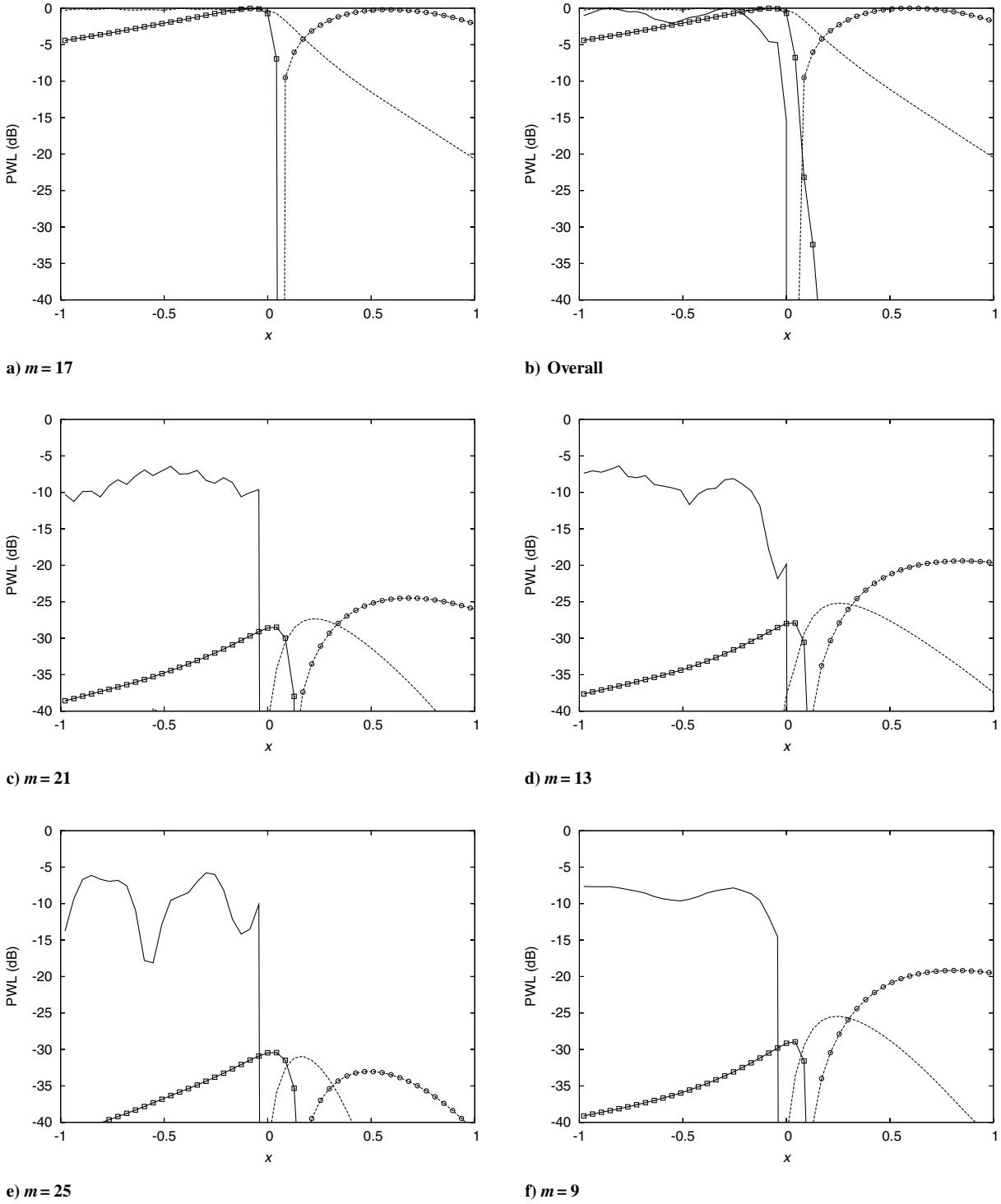

Fig. 6 Downstream/upstream axial power levels. Mode (17, 2). Duct mode scattering due to the large-splice liner. Inner cylinder (lines), outer cylinder (lines + symbols). Upstream levels (solid line), downstream levels (dashed line).

nozzle section. The nozzle radius is $r_0 = 1$ m and it is used as reference length throughout the paper by reporting only dimensionless lengths. The centerbody radius is $r_1 = 0.75$. For the axisymmetric cases, the computational domain extends from 0.75 to 5.75 in the radial direction and from -5 to 7 in the axial direction. For the three-dimensional cases, two meshes are considered: the first one extending from 0.75 to 2.75 in the radial direction and from -2 to 4 in the axial direction; the second one extending from 0.75 to 2.75 in the radial direction and from -2 to 2 in the axial direction. A Cartesian mesh with constant spacing along the axial and radial directions is employed. The two-dimensional domain is discretized by a 221×572 Cartesian grid, whereas the three-dimensional domains are discretized by $41 \times 142 \times 297$ and $65 \times 133 \times 297$ Cartesian-annular grids, respectively, obtained by performing 297 extrusion steps with constant angular spacing. The duct wall is modeled as a zero-thickness splitter duct by forcing a topological disconnection into the mesh. The unit normal vector to the wall is aligned with the radial direction at all the nodes of the splitter duct, the nozzle included. As discussed in [13], this corresponds to a no-model treatment of the boundary condition at the edge that is virtually located a half-grid segment downstream.

The bypass and external coaxial streams have Mach numbers $M_j = 0.45$ and $M_0 = 0.25$, respectively. Constant thermodynamic properties are assumed across the field ($p_0 = 10^5$ Pa,

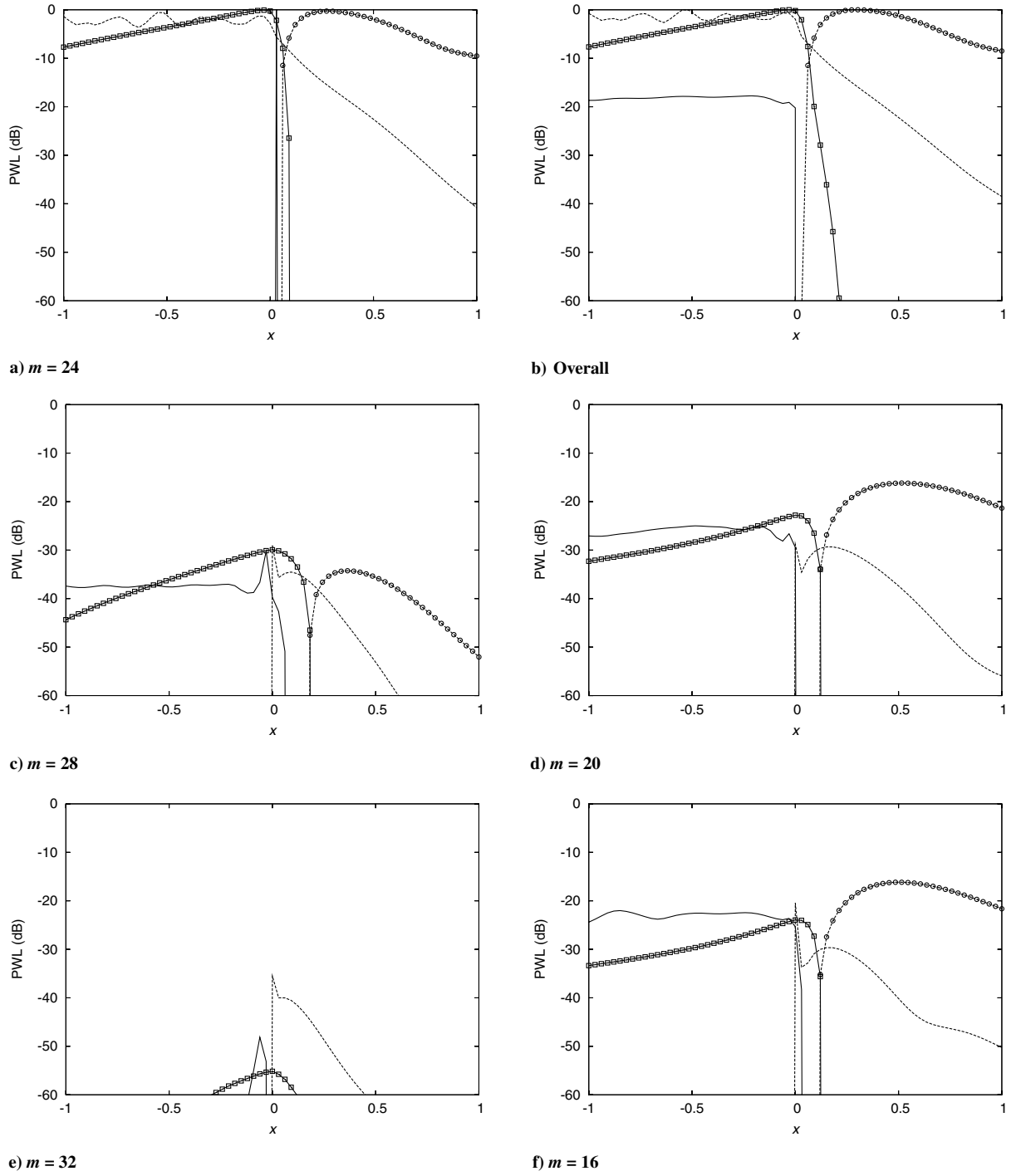

Fig. 7 Downstream/upstream axial power levels. Mode (24, 2). Duct mode scattering due to the large-splice liner. Inner duct (lines), outer duct (lines + symbols). Upstream levels (solid line), downstream levels (dashed line).

$\rho_0 = 1.16$ kg/m^3). Two inlet duct spinning modes are considered, with $m = 17$ and $m = 24$ azimuthal order, respectively, and equal radial order $n = 2$ ($n = 1$ denotes the lowest radial mode). For the three-dimensional cases, the modes (17, 2) and (24, 2) are computed by using the first and second mesh, respectively. All the simulations are carried out by considering an inlet power level corresponding to 100 dB (reference pressure $2 \cdot 10^{-5}$). The Helmholtz number is $kr_0 = 30$, corresponding to the cut-on ratios $\xi = 1.411$ and $\xi = 1.071$ for the modes (17, 2) and (24, 2), respectively. Computations are performed by considering both a rigid and a lined afterbody. The dimensionless impedance for the soft-wall case is $\mathcal{Z} = 2 + \mathrm{i}$ ($-\mathrm{i}\,\omega t$ convention).

The far-field directivity is computed at a distance $r_{\mathrm{FF}} = 100$ by performing a Kirchhoff integration upon a cylindrical surface of radius 2 and 1.1 for the axisymmetric and three-dimensional computation, respectively. The integration surfaces span the whole axial length of the computational domain, the axial PML buffers included. In the GFD code, two integral wave extrapolators are available: a frequency-domain porous Ffowcs–Williams and Hawkings (FW-H) extrapolator, obtained by a three-dimensional generalization of Lockard's approach [21], and a frequency-domain Kirchhoff wave extrapolator, obtained by applying Fourier and Galilean transformations to the time-domain solution by Farassat and Myers [22]. These are perfectly equivalent when the integration surface is in the linear propagation field [23]. However, the FW-H formulation is preferable when a wave equation for the acoustic velocity potential is computed, whereas the Kirchhoff formulation is preferable when a wave equation for the pressure perturbation is

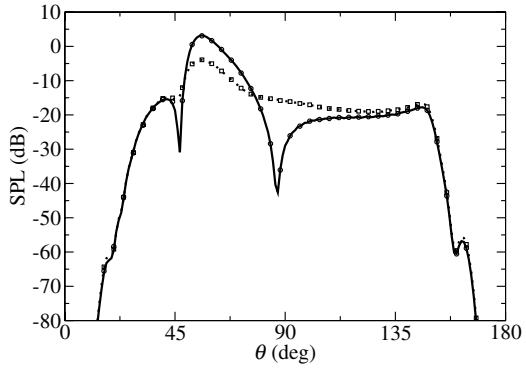

a) Mode (17,2)

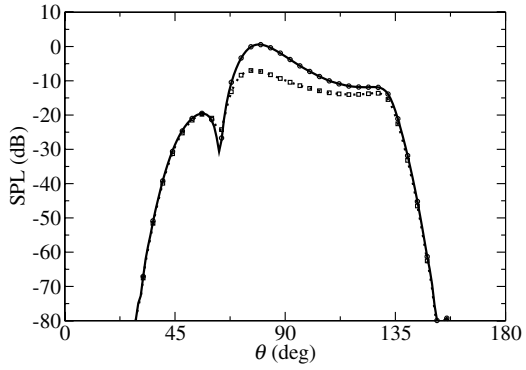

b) Mode (24,2)

Fig. 8 Far-field pressure directivity pattern (SPL_D). Mixing-layer refraction effects. Piecewise constant flow (lines), mixing-layer flow (lines + symbols), hard-wall (solid line), soft-wall (dashed line).

computed. The predicted far-field noise levels are plotted in sound pressure levels (SPL, reference pressure $2 \cdot 10^{-5}$) units corrected by the inlet sound power level, by the radial energy spreading, and by the root-mean-square factor $20\log(\sqrt{2}) \simeq 3$ dB by using the formula $SPL_D = SPL - 100 + 20\log(r_{FF}) + 3$. The directivity of SPL_D are compared with the directivity function $|D_p|^2$ defined in [14].

All the computations have been carried out by using PML buffers of thickness 0.7, and maximum damping constant $\sigma^{max} = 1.5$. Axisymmetric computations have been carried out by using a direct linear system solver, whereas three-dimensional computations have been carried out by using an iterative solver employing a standard BiCGstab-2 method and a preconditioned matrix. In agreement with the half-plane scattering problem investigated in [13], no instability waves have been observed in all the simulations performed, even though the acoustic wavelength is larger than the mixing-layer thickness in the edge region. On one side, this may be due to the fact that the bypass nozzle has zero thickness and consequently the mixing layer has zero initial thickness too. In fact, as pointed out by Barone and Lele [24], the use of a shear layer with initial infinitesimal thickness restricts the band of unstable frequencies. On the other side, the use of a harmonic discretization basis with wave number smaller than the wake vortical wave number prevents the excitation of the vortical mode, unless the mean flow reaches sonic conditions. In this case, the acoustic and vortical wave numbers reach a close value and, consequently, instabilities can occur even in the frequency domain, unless a direct linear system solver is used [9,25].

A. Method Verification

As a preliminary verification test, the analytical sound directivity pattern is compared with the axisymmetric and three-dimensional GFD results. All the axisymmetric results are grid-domain independent.

Results for the mode (17, 2) and a hard-wall afterbody are shown in Fig. 2a. The axisymmetric solution compares quite well with the analytical solution. The maximum error is 1.8 dB and occurs in the main diffraction peak, whereas the maximum angular deviation of the destructive interference direction close to 90 deg is less than 1 deg. Because of these differences, whose origin is unclear, the axisymmetric numerical solution, which is grid-domain independent, is better suited for evaluating the accuracy of the three-dimensional numerical solution. This is affected by a maximum error of 2 dB occurring in the backward diffraction lobe ($\theta > 90$ deg). This error is mainly due to an incomplete integration in the far-field extrapolation. In the axisymmetric computation, in fact, the length of the duct is two, instead of five as in the three-dimensional computation. The maximum angular deviation of the destructive interference direction close to 90 deg is about 3 deg, and it is due to a lack of discretization points close to the edge.

Results for the mode (17, 2) and a soft-wall afterbody are shown in Fig. 2b. The maximum difference between axisymmetric and three-dimensional GFD results is less than 1 dB, and the maximum angular deviation of the main diffraction lobe is less than 2 deg.

Results for the mode (24, 2) and a hard-wall afterbody are shown in Fig. 3a. As in the previous case, the axisymmetric solution compares quite well with the analytical solution. The maximum error is 2 dB and occurs in the backward diffraction lobe, whereas the maximum angular deviation of the destructive interference direction close to 63 deg is less than 1 deg. The comparison between the axisymmetric and three-dimensional solutions is quite good and the global error in the main lobe regions is less than 1 dB. Strong perturbations occur for the three-dimensional case close to extremities of the radiation arc, probably due to a convergence lack of the linear system solution. The solution is, however, well predicted over a dynamic range of about 50 dB.

Finally, results for the mode (24, 2) and a soft-wall afterbody are shown in Fig. 3b. Again, the maximum difference between axisymmetric and three-dimensional GFD results is less than 1 dB, and the maximum angular deviation of the main diffraction lobe is less than 1 deg.

B. Effects Due to a Spliced Liner on the Bypass Duct Afterbody

In this section, some effects of a spliced liner on the afterbody are illustrated. Four equally spaced splices are considered and computations are performed for two values of the splice thickness: $6.37 \cdot 10^{-2}$ and $12.74 \cdot 10^{-2}$. These are discretized with four and eight grid segments, respectively, in the azimuthal direction.

Three-dimensional sound directivity patterns for the mode (17, 2) are shown in Fig. 4a. The zero-splice liner reduces the main radiation peak of 7.1 dB, whereas the small- and large-splice liners reduce the main radiation peak of 5.5 dB and 5.1 dB, respectively. The performance degradation due to a large-splice liner is therefore about 2 dB. By contrast, the effect of the liner is to increase the noise levels in the backward radiation arc ($\theta > 90$ deg). This is due to the edge-diffraction of the wave component generated at the axial discontinuity of the liner on the centerbody. In fact, for a spliced liner, this wave component is weaker, resulting in slightly lower noise levels.

Three-dimensional sound directivity patterns for the mode (24, 2) are shown in Fig. 4b. The zero-splice liner reduces the main radiation peak of 8.0 dB, whereas the small- and large-splice liners reduce the main radiation peak of 6.8 dB and 6.4 dB, respectively. The performance degradation due to a large-splice liner is about 1.6 dB. In addition, the effect of the splices is to increase the forward radiation peak of about 5 dB. This is due to the modal scattering into modes with lower azimuthal order.

To better highlight the effects of the modal scattering due to rigid splices, an azimuthal Fourier decomposition of the transmitted power levels across two coaxial cylinders is carried out. The analysis is the same carried out by Tester et al. [3], based on the acoustic power definition by Morfey [26]. The inner coaxial cylinder extends radially from 0.75 to 1, whereas the outer one extends radially from 1 to 2. For each section of the cylinder, azimuthal Fourier components of the acoustic pressure and velocity are computed. These are used to compute the corresponding Fourier components of the acoustic

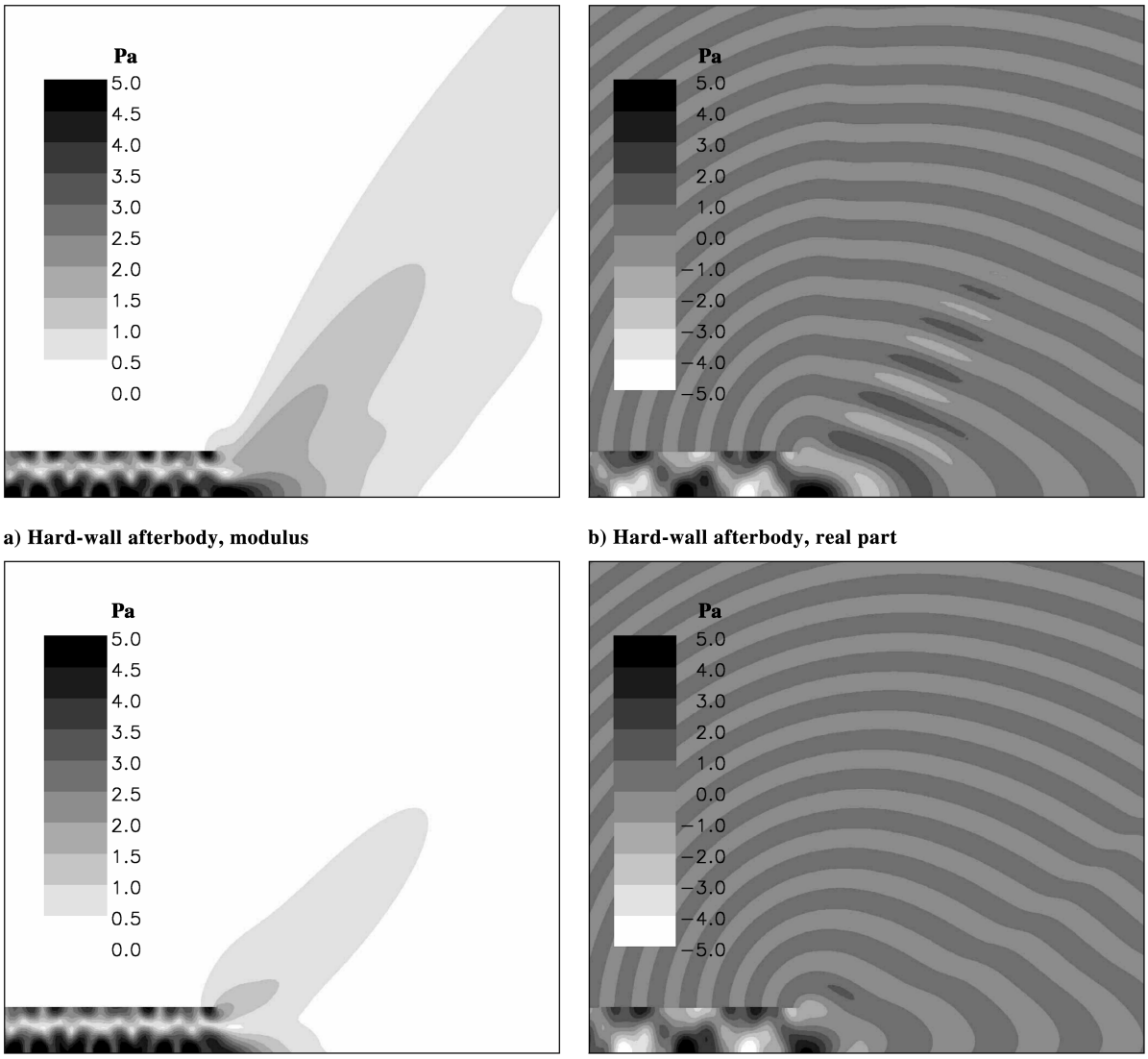

a) Hard-wall afterbody, modulus

b) Hard-wall afterbody, real part

c) Soft-wall afterbody, modulus

d) Soft-wall afterbody, real part

Fig. 9 Pressure perturbation contours in the presence of a mixing-layer flow. Hard-wall vs soft-wall results. Mode (17, 2).

intensity vector that is integrated over the annular section. Positive (downstream) and negative (upstream) contributions are plotted separately. The total downstream transmitted axial power level is computed by summation over all the positive Fourier components. The maximum value along the axial direction of the total downstream transmitted axial power level is used to normalize the power level of each downstream transmitted Fourier component. The same normalization strategy is carried out for the upstream Fourier components. An overall power level is finally defined by summating the magnitudes of the downstream and upstream transmitted Fourier components and integrating over all the Fourier components. This overall value is normalized by the maximum overall power level occurring along the cylinder axis.

In Fig. 5a, the normalized overall axial power levels for the duct mode (17, 2) are plotted for the two coaxial cylinders. Results obtained for a zero-splice liner are compared with those obtained for the large-splice liner. The effect due to the splices is to increase the downstream transmitted power levels along the inner cylinder and to decrease the backward diffracted power levels along the outer cylinder. This confirms that a smoother axial impedance transition results in a weaker diffraction in the backward observation arc, as observed in Fig. 4a. The same behavior can be observed for the duct mode (24, 2) in Fig. 5b.

In Fig. 6, the normalized downstream and upstream axial power levels for the duct mode (17, 2) are plotted. Levels are referred to the maximum downstream/upstream levels over all the Fourier components occurring in the corresponding annular cylinder. In agreement with the theoretical result of [3], the incident mode 17 is scattered into the modes $17 \pm i \cdot 4$ ($i = 1, 2, \ldots$). It is interesting to observe that the outer upstream components (diffracted by the edge) of the scattered modes have comparable levels.

In Fig. 7, the normalized downstream and upstream axial power levels for the duct mode (24, 2) are plotted. Again, in agreement with the theoretical result of [3], the incident mode 24 is scattered into the modes $24 \pm i \cdot 4$ ($i = 1, 2, \ldots$). It is interesting to observe that the lower-order Fourier components $m = 16$ and $m = 20$ have significant downstream levels that can justify the observed increase of the forward radiation lobe of Fig. 5b.

C. Effects Due to a Mixing Layer

In this section, axisymmetric results are presented for the bypass duct radiation in the presence of a mixing layer. The self-similar velocity profile

$$U(x, r) = \frac{U_j + U_0}{2}\left[1 - \frac{U_j - U_0}{U_j + U_0}\,\mathrm{erf}\left(\eta\,\frac{r - r_0}{x}\right)\right] \qquad (11)$$

is introduced downstream of the bypass nozzle. The corresponding density profile is computed by using the Crocco–Busemann relation. A value $\eta = 13$ of the mixing constant is used. The far-field

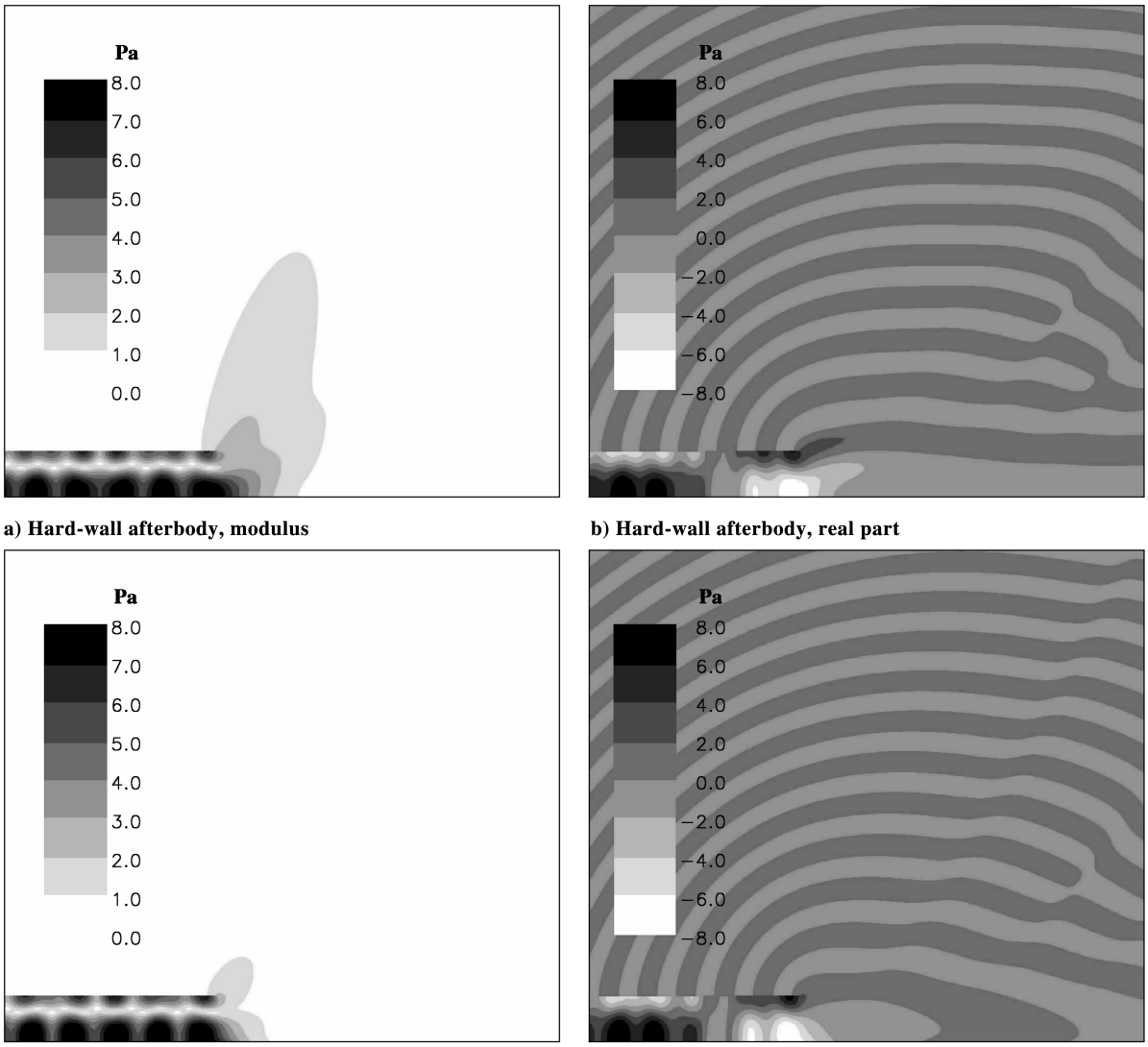

a) Hard-wall afterbody, modulus **b) Hard-wall afterbody, real part**

c) Soft-wall afterbody, modulus **d) Soft-wall afterbody, real part**

Fig. 10 Pressure perturbation contours in the presence of a mixing-layer flow. Hard-wall vs soft-wall results. Mode (24, 2).

directivity patterns for the inlet duct modes (17, 2) and (24, 2) are plotted in Fig. 8. A comparison with the piecewise base-flow solution ($\eta \to \infty$) shows that the mixing layer has a negligible effect on the far-field noise levels for both the hard-wall and soft-wall afterbody. The same conclusion has been drawn in [13] for a two-dimensional case.

Finally, Figs. 9 and 10 show the contour plots of the pressure perturbation for the inlet duct modes (17, 2) and (24, 2), respectively.

V. Conclusions

This paper finalizes the verification process of the Green's function discretization of a homogeneous linearized Lilley's equation in the frequency domain. Numerical results obtained by solving both the axisymmetric and the three-dimensional wave equations have been compared with a Wiener–Hopf analytical solution. The agreement is quite satisfactory for the axisymmetric case. The three-dimensional results, obtained by using coarser grids and quite less extended computational domains, compare fairly well with the reference results. As an illustrative example of an applicative study, the effects due to a spliced liner on the afterbody have been investigated. The degradation of the liner performances seems to be less dramatic than that occurring in a lined duct. Finally, to show the applicability of the method to a more realistic sheared flow, the sound propagation in the presence of a mixing layer have been computed. No significant refraction effects have been observed.

A theoretical study has been recently undertaken to model a source term on the base of statistical flow quantities. A stochastic method based on averaging different realizations of the acoustic fields, each obtained by using stochastic phase perturbations of the source distribution, is under development.

Acknowledgments

The authors wish to thank Jeremy Astley and Gwenael Gabard of University of Southampton, and Sjoerd Rienstra and Ahmet Demir of Eindhoven University of Technology for fruitful discussions about the analytical solutions.

References

[1] Li, X., Schoenwald, N., Yan, J., and Thiele, F., "A Numerical Study on the Acoustic Radiation from a Scarfed Intake," AIAA Paper 2003-3245, 2003.

[2] Di Francescantonio, P., Casalino, D., and De Mercato, L., "Aeroacoustic Design of Aero-Engine Intake Liners," AIAA Paper 2005-2942, May 2005.

[3] Tester, B. J., Powles, C. J., Baker, N. J., and Kempton, A. J., "Scattering of Sound by Liner Splices: A Kirchhoff Model with Numerical Verification," *AIAA Journal*, Vol. 44, No. 9, 2006, pp. 2009–2017. doi:10.2514/1.17678

[4] Di Francescantonio, P., and Casalino, D., "Green's Function Discretization Scheme for Sound Propagation in Nonuniform Flows," *AIAA Journal*, Vol. 37, No. 10, 1999, pp. 1161–1172.

[5] Casalino, D., Roger, M., and Jacob, M., "Prediction of Sound Propagation in Ducted Potential Flows Using Green's Function Discretization," *AIAA Journal*, Vol. 42, No. 4, 2004, pp. 736–744.
[6] Casalino, D., Genito, M., and Visingardi, A., "Numerical Analysis of Airframe Noise Scattering Effects in Tilt-Rotor Systems," *AIAA Journal*, Vol. 45, No. 4, 2007, pp. 751–759. doi:10.2514/1.24605
[7] Pierce, A. D., "Wave Equation for Sound in Fluids with Unsteady Inhomogeneous Flow," *Journal of the Acoustical Society of America*, Vol. 87, No. 6, 1990, pp. 2292–2299. doi:10.1121/1.399073
[8] Bergliaffa, S. E. P., Hibberd, K., Stone, M., and Visser, M., "Wave Equation for Sound in Fluids with Vorticity," *Physica D*, Vol. 191, Nos. 1–2, 2004, pp. 121–136. doi:10.1016/j.physd.2003.11.007
[9] Casalino, D., and Bodony, D., "Green's Function Discretization of Pridmore-Brown Wave Operator," *Proceedings of the Summer Program 2006*, Center for Turbulence Research, Stanford Univ., Stanford, CA, 2006, pp. 547–558.
[10] Lilley, G. M., "On the Noise from Jets," AGARD CP-131, 1974.
[11] Li, X., Schemel, C., Michel, U., and Thiele, F. H., "Azimuthal Sound Mode Propagation in Axisymmetric Flow Ducts," *AIAA Journal*, Vol. 42, No. 10, 2004, pp. 2019–2027.
[12] Redonnet, S., Manoha, E., and Kenning, O., "Numerical Simulation of the Downstream Fan Noise of 3D Coaxial Engines," AIAA Paper 2005-2816, 2005.
[13] Genito, M., Casalino, D., and Botte, V., "Numerical Modelling of Sound Diffraction at a Half Plane Trailing Edge," AIAA Paper 2007-3503, 2007.
[14] Gabard, G., and Astley, R. J., "Theoretical Model for Sound Radiation from Annular Jet Pipes: Far- and Near-Field Solutions," *Journal of Fluid Mechanics*, Vol. 549, 2006, pp. 315–341. doi:10.1017/S0022112005008037
[15] Demir, A., and Rienstra, S. W., "Sound Radiation from an Annular Duct with Jet Flow and a Lined Centerbody," AIAA Paper 2006-2718, 2006.
[16] Goldstein, M. E., "Aeroacoustics of Turbulent Shear Flows," *Annual Review of Fluid Mechanics*, Vol. 16, 1984, pp. 263–285. doi:10.1146/annurev.fl.16.010184.001403
[17] Colonius, T., Lele, S. K., and Moin, P., "Sound Generation in a Mixing Layer," *Journal of Fluid Mechanics*, Vol. 330, 1997, pp. 375–409. doi:10.1017/S0022112096003928
[18] Goldstein, M. E., "An Exact Form of Lilley's Equation with a Velocity Quadrupole/Temperature Dipole Source Term," *Journal of Fluid Mechanics*, Vol. 443, 2001, pp. 231–236. doi:10.1017/S002211200100547X
[19] Goldstein, M. E., "A Generalized Acoustic Analogy," *Journal of Fluid Mechanics*, Vol. 488, 2003, pp. 315–333. doi:10.1017/S0022112003004890
[20] Myers, M. K., "On the Acoustic Boundary Condition in the Presence of Flow," *Journal of Sound and Vibration*, Vol. 71, No. 3, 1980, pp. 429–434.
[21] Lockard, D. P., "An Efficient, Two-Dimensional Implementation of the Ffowcs Williams and Hawkings Equation," *Journal of Sound and Vibration*, Vol. 229, No. 4, 2000, pp. 897–911. doi:10.1006/jsvi.1999.2522
[22] Farassat, F., and Myers, M. K., "Extension of Kirchhoff's Formula to Radiation from Moving Surfaces," *Journal of Sound and Vibration*, Vol. 123, No. 3, 1988, pp. 451–461. doi:10.1016/S0022-460X(88)80162-7
[23] Brentner, K. S., and Farassat, F., "Analytical Comparison of the Acoustic Analogy and Kirchhoff Formulation for Moving Surfaces," *AIAA Journal*, Vol. 36, No. 8, 1998, pp. 1379–1386.
[24] Barone, M. F., and Lele, S. K., "Receptivity of the Compressible Mixing Layer," *Journal of Fluid Mechanics*, Vol. 540, 2005, pp. 301–335. doi:10.1017/S0022112005005884
[25] Agarwal, A., Morris, P. J., and Mani, R., "Calculation of Sound Propagation in Nonuniform Flows: Suppression of Instability Waves," *AIAA Journal*, Vol. 42, No. 1, 2004, pp. 80–88.
[26] Morfey, C. L., "Sound Transmission and Generation in Ducts with Flow," *Journal of Sound and Vibration*, Vol. 14, No. 1, 1971, pp. 37–55. doi:10.1016/0022-460X(71)90506-2

R. So
Associate Editor